Study of Wave Group Velocity Estimation From Inhomogeneous Sea-Surface Image Sequences by Spatiotemporal Continuous Wavelet Transform

Laurence Zsu-Hsin Chuang and Li-Chung Wu

***Abstract*—In this paper, a new image processing technique is introduced for the analysis of consecutive ocean wave images by spatiotemporal continuous wavelet transform (STCWT) using the Morlet wavelet as the mother wavelet. This technique, which has been adapted to give a full time–frequency and spatiofrequency representation of ocean surface waves from remotely captured wave image sequences, provides more detailed information from wave-field measurements than the traditional Fourier transform (FT) method. A series of numerical simulations of wave image sequences was analyzed to justify the algorithm and to present quantitative theoretical results on the propagation of ocean waves for normal incidence, diffraction, reflection, and shoaling in coastal areas. The comparisons of these estimates to simulated conditions for several wave parameters show that the wavelet theory is applicable to the identification of wave spectra from inhomogeneous sea-surface image sequences.**

***Index Terms*—Inhomogeneous sea-surface image sequences, spatiotemporal continuous wavelet transform (STCWT), wave group velocity.**

I. Introduction

OCEAN waves exhibit an oscillating pattern that is a function of space and time. The wave spectrum has been one of the most useful tools for the investigation of wave characteristics since the 1950s [1]. To obtain the spectrum from a time series or a wave record in the space domain, the Fourier transform (FT) technique has been widely applied. However, we require information on the relative intensities (but not the spatial or temporal locations) of the particular frequency (spatial frequency) components to implement the FT technique. Such information is insufficient in the cases of nonstationary or inhomogeneous signals, such as surface waves that change in a relatively short period of time or over a short spatial distance. When the time/space localization of the spectral components is required, several studies have already shown the successful implementation of the wavelet transform (WT) to reveal ocean wave characteristics from 1-D time-series records [2], [3] and 2-D wave images [4], [5].

Manuscript received February 22, 2012; revised March 23, 2013; accepted June 11, 2013. Date of publication November 13, 2013; date of current version July 10, 2014. This work was supported by the National Science Council in Taiwan under Grants NSC 97-2218-E-006-010 and NSC 101-2221-E-006-046.

Associate Editor: J. F. Lynch.

The authors are with the Coastal Ocean Monitoring Center, National Cheng Kung University, Tainan 70010, Taiwan (e-mail: jackalson18@gmail.com).

Color versions of one or more of the figures in this paper are available online at http://ieeexplore.ieee.org.

Digital Object Identifier 10.1109/JOE.2013.2269211

Following the same principles as those of the 1-D and 2-D wavelet transforms, Murenzi extended the theory of wavelet transform to multiple dimensions [6]. Then, Duval-Destin and Murenzi proposed a slightly different generalization scheme to consider motion analysis [7]. This scheme represents the first continuous spatiotemporal wavelet transform to be developed. To consider additional motion parameters, such as the vectored speed and uniform rotational and accelerated motion in the analysis of image sequences, Leduc proposed another method called the Galilean wavelet transform to analyze spatiotemporal signals [8]. The Galilean wavelets define a family of nonseparable filters that are suitable for motion representation, while the wavelet family proposed by Duval-Destin and Murenzi [7] is separable.

Several remote sensing technologies, such as nautical radar monitoring and stereophotogrammetry, have proven their ability to represent spatiotemporal sea-surface wave patterns [9], [10]. Of the ocean wave parameters that can be extracted from spatiotemporal sea-surface images, the wave group velocity is one of the most significant parameters describing the propagation of a group of ocean waves because it represents the rate at which energy is transferred by a train of propagating waves [11]. The wave group velocity is also important to both oceanography and coastal engineering applications, such as the study of the wave shoaling coefficient, the wave energy flux, the long shore sediment transport equation, the mild-slope equation, and the wave numerical mode [12]. The wave field is one of the most useful tools for the extraction of wave group velocity information by estimating the relationship between different wave features in the spatiotemporal domain. For the homogeneous wave-field scenario, the FT is clearly the most useful tool for wave-field analysis and wave group velocity estimation. However, inhomogeneity is often unavoidable in near-shore and shallow-water wave fields. For the data requirements of coastal engineering, coastal area protection and management, and oceanic recreation, the area of interest is always within several kilometers of the land. This proximity implies that we must often consider the ocean environment in shallow-water areas. However, the estimation of ocean wave motion parameters from inhomogeneous spatiotemporal sea-surface image sequences has received little attention until now.

This study was motivated by the work published in [7], [13], and [14]. We considered the application of the spatiotemporal continuous wavelet transform (STCWT) to the estimation of wave group velocity from continuous sea-surface image sequences. To verify whether the tool is best adapted to the problem at hand, we must properly calibrate the procedures

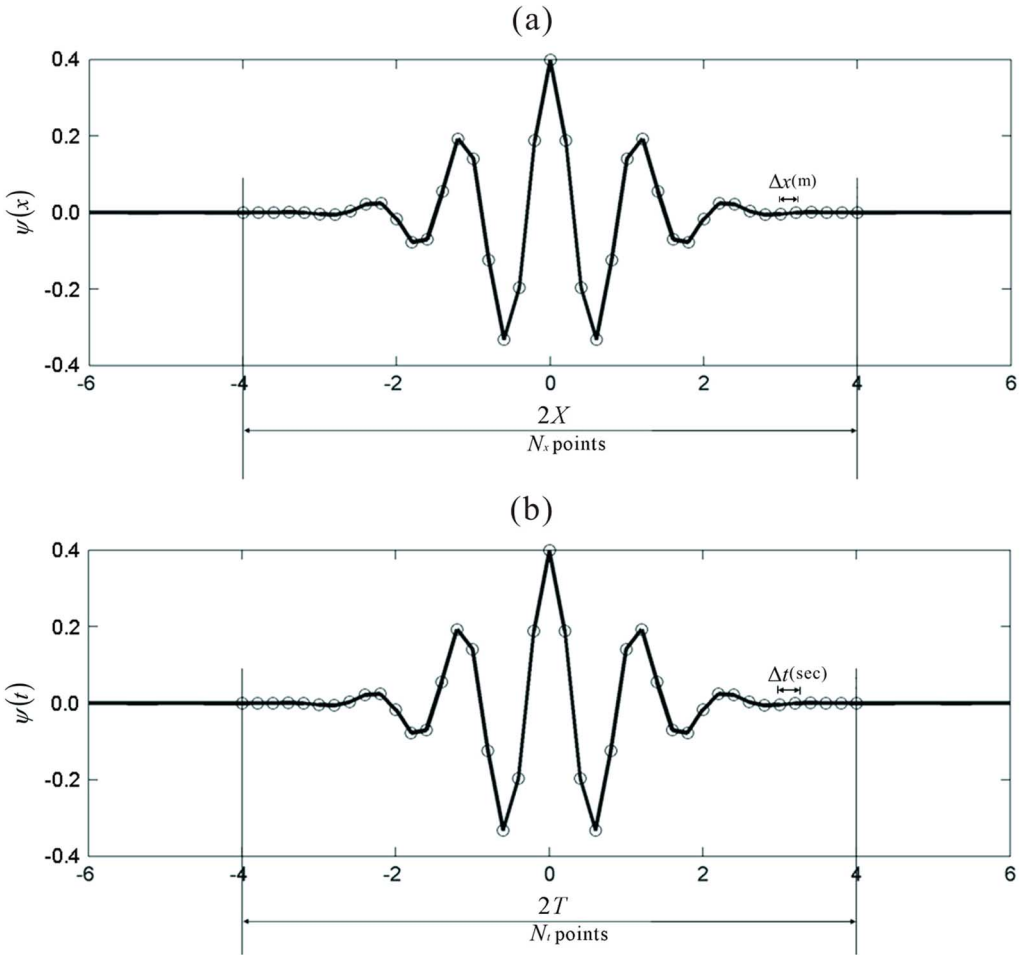

Fig. 1. Correspondence between sampled points of the physical quantity and the sampled points of the wavelet.

and quantitatively evaluate their performances. Regular and irregular simulated spatiotemporal sea-surface image sequences are employed in our study to confirm the practicability of our method.

II. Theoretical Preliminaries

The 1-D wavelet transform theory and its application to ocean surface waves was introduced and discussed in [2]. In this section, we focus on reviewing the theory of the STCWT, which was introduced in [13] and [14]. We then develop an STCWT algorithm to derive the wave group velocity of ocean waves.

A. Spatiotemporal Continuous Wavelet Transform

The WT is similar to the FT in that it breaks signals into their constituents. However, the WT breaks the signals into different kinds of wavelets, which are scaled, shifted, rotated, and speed-tuned versions of a prechosen mother wavelet. This approach allows exceptional localization in both the time and space domains via translations of the mother wavelet and in the scale (frequency/wave number) domain via dilations and rotations.

Consider a (2+1)-dimensional signal, such as a sea-surface image sequence in two spatial domains plus a time domain, $s(\vec{\boldsymbol{x}},t) = s(x,y,t)$. The discrete values of $s(\vec{\boldsymbol{x}},t)$ correspond to the sea-surface elevation of each pixel at different locations and instants. We could represent any finite energy signal by

$$\|s\|^2 = \iint |s(\vec{\boldsymbol{x}},t)|^2 \,\mathrm{d}^2\vec{\boldsymbol{x}}\,\mathrm{d}t < \infty. \tag{1}$$

This representation means that the complex-valued function defined on the real plane is square integrable. The FT of $s(\vec{\boldsymbol{x}},t)$ is defined by

$$\hat{s}(\vec{\boldsymbol{k}},\omega) = (2\pi)^{-1.5} \iint s(\vec{\boldsymbol{x}},t)\exp[-\mathrm{i}(\vec{\boldsymbol{k}}\cdot\vec{\boldsymbol{x}} - \omega t)]\,\mathrm{d}^2\vec{\boldsymbol{x}}\,\mathrm{d}t \tag{2}$$

in which ω is the angular frequency, $\vec{\boldsymbol{k}}$ is the wave number (or spatial frequency) for the fields of oceanography and coastal engineering, and $\vec{\boldsymbol{k}}\cdot\vec{\boldsymbol{x}} = k_x x + k_y y$. Here, k_x and k_y are the wave-number components in the x- and y-domains, respectively. The corresponding STCWT of the signal of interest is defined as the inner product of the signal $s(\vec{\boldsymbol{x}},t)$ and the transformed wavelet $\psi_{a,c,\theta;\vec{\boldsymbol{b}},\tau}$ as follows:

$$S(a,c,\theta;\vec{\boldsymbol{b}},\tau) = \frac{1}{\sqrt{C_\psi}}\left\langle \psi_{a,c,\theta;\vec{\boldsymbol{b}},\tau} | s(\vec{\boldsymbol{x}},t)\right\rangle \tag{3}$$

where the complex-valued wavelet function $\psi_{a,c,\theta;\vec{\boldsymbol{b}},\tau}$, which is localized in the space and time domains, is the shifted,

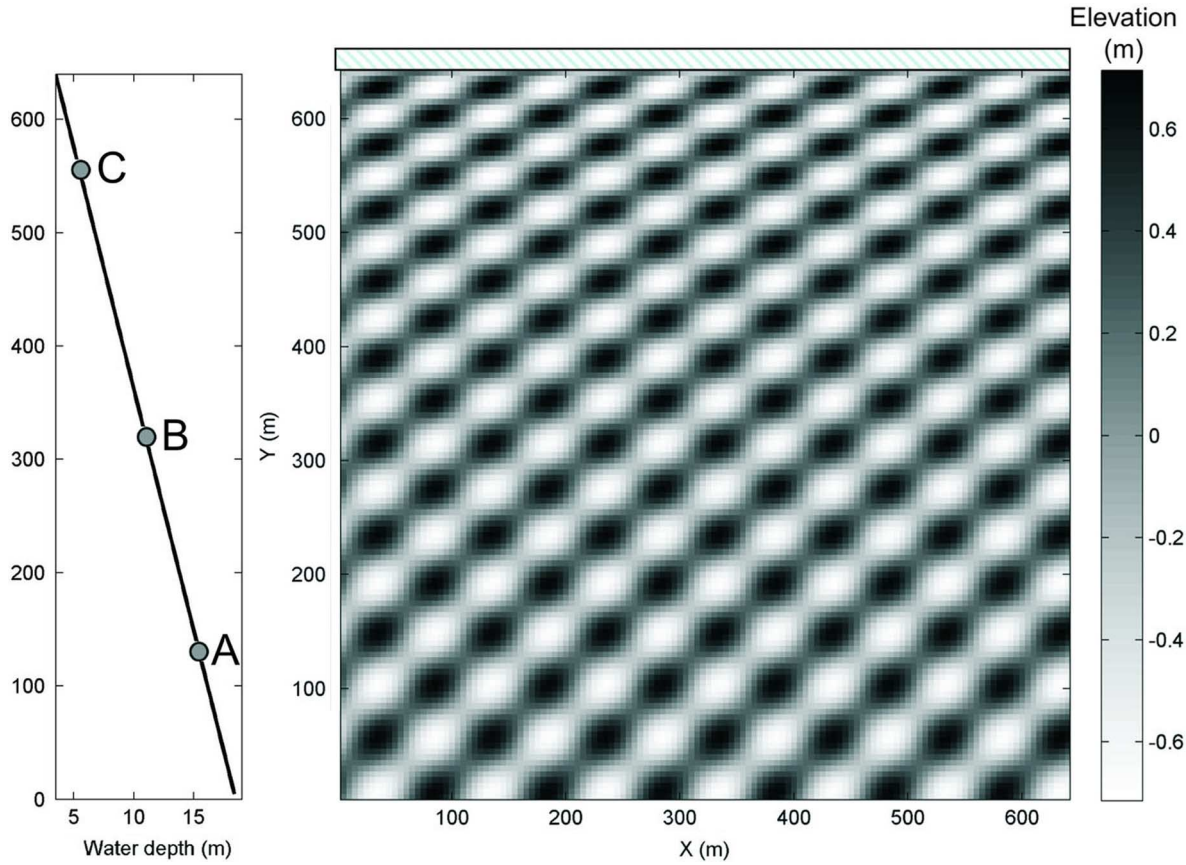

Fig. 2. Inhomogeneous wave image with wave reflection, refraction, and shoaling.

scaled, rotated, and speed-tuned version of the prechosen mother wavelet $\psi(\vec{\boldsymbol{x}}, t)$. The mother wavelet was defined as follows in [14] and [15]:

$$\psi_{a,c,\theta;\vec{\boldsymbol{b}},\tau}(\vec{\boldsymbol{x}}, t) = a^{-3/2} \times \psi\left(a^{-1}c^{-1/3}\boldsymbol{r}_{-\theta}\cdot(\vec{\boldsymbol{x}} - \vec{\boldsymbol{b}}), a^{-1}c^{2/3}(t-\tau)\right). \quad (4)$$

The translation parameters $\vec{\boldsymbol{b}}$ and τ correspond to the given position of the wavelet as it shifts through the space and time domains. The scaling parameter a, which is a nondimensional scale factor, is associated with the size of the object of interest and operates in the same way in both time and space. The factor a^{-1} is a normalization that gives all dilated versions of the mother wavelet the same energy, i.e., it is the ratio of the size of the dilated wavelet to the size of the mother wavelet. The speed tuning parameter c is directly associated with a proportional change of the velocity magnitude of the moving wavelet, while the velocity orientation remains unchanged. This speed tuning parameter is a key factor in the detection of the wave phase speed and wave group velocity from the sea-surface image sequences in our study. The rotation matrix $\boldsymbol{r}_{-\theta}$ with a rotation angle θ, which rotates the spatial coordinates of the wavelet around the temporal axis, is usually defined as follows:

$$\boldsymbol{r}_{-\theta} = \begin{pmatrix} \cos\theta & \sin\theta \\ -\sin\theta & \cos\theta \end{pmatrix}, \qquad 0 \le \theta < 2\pi. \quad (5)$$

Equation (3) can now be expressed as follows to display the wavelet theory formula more clearly:

$$S(a, c, \theta; \vec{\boldsymbol{b}}, \tau) = \frac{1}{\sqrt{C_\psi}} \int\int a^{-3/2} \times \psi^*\left(a^{-1}c^{-1/3}\boldsymbol{r}_{-\theta}\cdot(\vec{\boldsymbol{x}} - \vec{\boldsymbol{b}}), a^{-1}c^{2/3}(t-\tau)\right) \times s(\vec{\boldsymbol{x}}, t)\,\mathrm{d}^2\vec{\boldsymbol{x}}\,\mathrm{d}t \quad (6)$$

where ψ^* is the complex conjugate of the mother wavelet function ψ. Different mother wavelet functions have been proposed and applied for various applications by different studies. Regardless of the type of equation, all mother wavelet functions must satisfy the following admissibility condition:

$$C_\psi = (2\pi)^3 \int\int_{\mathrm{R^2R}} \frac{|\hat{\psi}(\vec{\boldsymbol{k}}, \omega)|^2}{|\vec{\boldsymbol{k}}|^2|\omega|}\,\mathrm{d}^2\vec{\boldsymbol{k}}\,\mathrm{d}\omega < \infty \quad (7)$$

in which $\hat{\psi}(\vec{\boldsymbol{k}}, \omega)$ is the FT of the wavelet function $\psi(\vec{\boldsymbol{x}}, t)$. To implement (6), we use a spatiotemporal Morlet wavelet as the mother wavelet throughout the implementation procedures. The well-known and most commonly used Morlet wavelet is a directionally selective wavelet function that has been popularly adopted as a wavelet transform for signal analysis [16] and ocean signal analysis [17]. The spatiotemporal Morlet wavelet

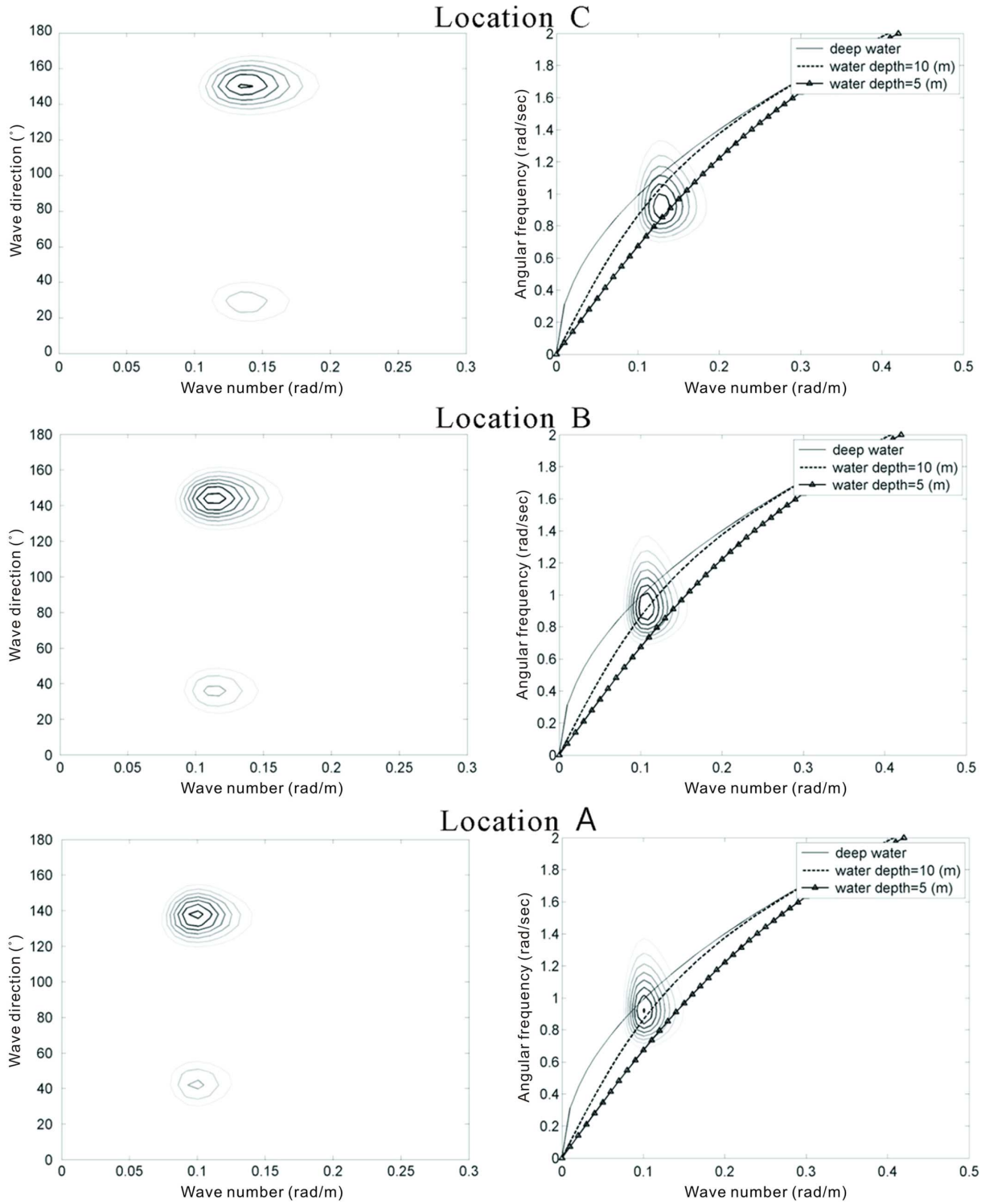

Fig. 3. Wave spectra $S(k,\theta)$ and $S(\omega,k)$, which were extracted from different locations of the inhomogeneous wave image from Fig. 2.

is defined in the following complex-valued form, as shown in [14]:

$$\begin{aligned}\psi(\vec{\boldsymbol{x}},t) &= \Big[\exp(\mathrm{i}\vec{\boldsymbol{k}}_0\cdot\boldsymbol{A}^{-1}\cdot\vec{\boldsymbol{x}})\exp(-0.5|\boldsymbol{A}^{-1}\cdot\vec{\boldsymbol{x}}|^2) \\ &\quad - \exp(-0.5|\boldsymbol{A}^{-1}\cdot\vec{\boldsymbol{x}}|^2)\exp(-0.5|\vec{\boldsymbol{k}}_0|^2)\Big] \\ &\quad \times\big[\exp(\mathrm{i}\omega_0 t)\exp(-0.5t^2) - \exp(-0.5t^2)\exp\big(-0.5\omega_0^2\big)\big]. \end{aligned} \tag{8}$$

A typical anisotropy matrix $\boldsymbol{A}$ is defined as $\varepsilon \geq 1$, as follows:

$$\boldsymbol{A} = \begin{bmatrix} \varepsilon^{-0.5} & 0 \\ 0 & 1 \end{bmatrix}. \tag{9}$$

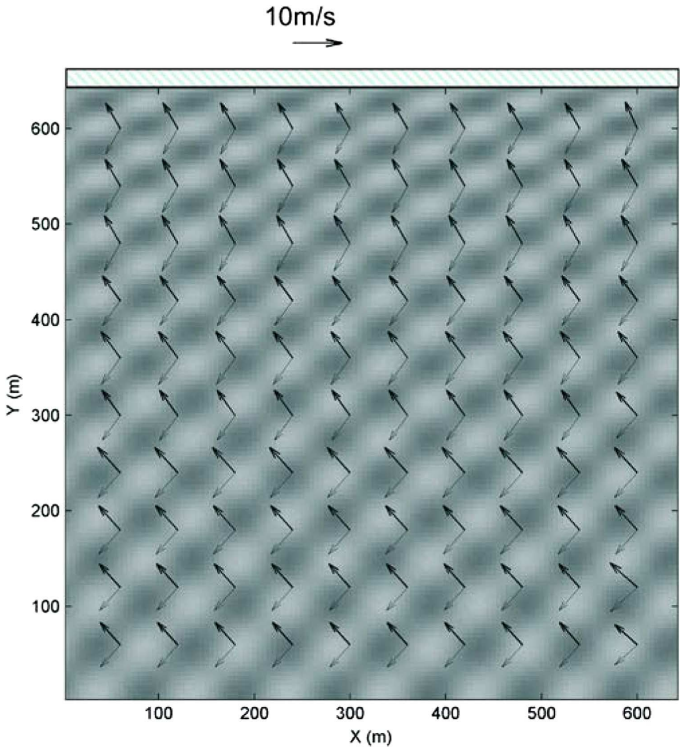

Fig. 4. The wave group velocity estimated results from different locations of the inhomogeneous wave image by the wavelet transform. The bold arrows indicate the estimated results of incident waves; the thin arrows indicate the reflected waves.

Our previous study revealed that $\varepsilon = 1$ is suitable for sea-surface image analysis [18]. Alternatively, the mother wavelet function can also be expressed in the wave-number frequency domain as follows:

$$\hat{\psi}(\vec{\boldsymbol{k}}, \omega) = \left(\exp(-0.5|\boldsymbol{A} \cdot \vec{\boldsymbol{k}} - \vec{\boldsymbol{k}}_0|^2) - \exp\left(-0.5(|\boldsymbol{A} \cdot \vec{\boldsymbol{k}}|^2 |\vec{\boldsymbol{k}}_0|^2)\right)\right) \times \left(\exp\left(-0.5|\omega - \omega_0|^2\right) - \exp\left(-0.5(\omega^2 + \omega_0^2)\right)\right) \tag{10}$$

in which $\vec{\boldsymbol{k}}_0 = (k_{0_x}, k_{0_y})$ and ω_0 are the center wave number and the frequency of the mother wavelet, respectively. Jordan *et al.* [19] suggested that $\omega_0 \in [5, 6]$ to access the admissibility condition of the wavelet function. Because of the similarity of the mother wavelet function in the time and space domains, we set the value of $\vec{\boldsymbol{k}}_0$ to lie within this range as well. However, the direction of the wavelet function in the space and wave-number domains is influenced by the nonzero values of k_{0_x} and k_{0_y}. Because the matrix $\boldsymbol{r}_{-\theta}$ defined by (5) was applied to control the direction of the wavelet function, k_{0_y} can be set equal to zero. In this paper, we use $\omega_0 = 6$ and $\vec{\boldsymbol{k}}_0 = (6, 0)$ to analyze sea-surface image sequences with the wavelet functions. In Section IV, we will discuss the influence of the values of $\vec{\boldsymbol{k}}_0$ and ω_0 on the wavelet window widths in different domains.

If $|\vec{\boldsymbol{k}}_0|$ and ω_0 are large enough (typically, $|\vec{\boldsymbol{k}}_0| \geq 6$ and $\omega_0 \geq 6$) the second terms in (8) and (10) are small enough to be neglected. Now, the Morlet wavelet can be simplified as follows:

$$\psi(\vec{\boldsymbol{x}}, t) = \exp(\mathrm{i}\vec{\boldsymbol{k}}_0 \cdot \boldsymbol{A}^{-1} \cdot \vec{\boldsymbol{x}}) \exp(-0.5|\boldsymbol{A}^{-1} \cdot \vec{\boldsymbol{x}}|^2) \times \exp(\mathrm{i}\omega_0 t) \exp(-0.5t^2) \tag{11}$$

in the spatiotemporal domain, or it can be equivalently simplified in the following manner:

$$\hat{\psi}(\vec{\boldsymbol{k}}, \omega) = \exp(-0.5|\boldsymbol{A} \cdot \vec{\boldsymbol{k}} - \vec{\boldsymbol{k}}_0|^2) \exp\left(-0.5|\omega - \omega_0|^2\right) \tag{12}$$

in the wave-number frequency domain. Both expressions approximate the modulated Gaussian or Gabor filters. Examples of the real and imaginary parts of (11) in the spatial domain and the transformed wavelets influenced by the rotation matrix $\boldsymbol{r}_{-\theta}$ at different angles are illustrated in [5, Figs. 1 and 2]. The corresponding wavelet of (12) in the wave-number domain is also depicted in [5, Fig. 3].

The simplest algorithm for implementation of (6) is direct numerical integration, but this approach is time consuming. A better solution is to execute the STCWT by taking advantage of the fast FT to compute the continuous wavelet transform efficiently in the wave-number (spatial frequency) frequency domain. Thus, the algorithm for STCWT in the spatiotemporal domain can be manipulated in the wave-number frequency domain by

$$\begin{aligned} S(a, c, \theta; \vec{\boldsymbol{b}}, \tau) &= \frac{1}{\sqrt{C_\psi}} \left\langle \hat{\psi}_{a,c,\theta;\vec{\boldsymbol{b}},\tau}(\vec{\boldsymbol{k}}, \omega) | \hat{s}(\vec{\boldsymbol{k}}, \omega) \right\rangle \\ &= \frac{1}{\sqrt{C_\psi}} \int\int \Big[a^{3/2} \exp(-\mathrm{i}(\vec{\boldsymbol{k}} \cdot \vec{\boldsymbol{b}} + \omega\tau)) \times \hat{\psi}^*(ac^{1/3}\boldsymbol{r}_{-\theta} \cdot (\vec{\boldsymbol{k}}), ac^{-2/3}\omega) \hat{s}(\vec{\boldsymbol{k}}, \omega)\Big] \times \mathrm{d}^2\vec{\boldsymbol{k}}\, \mathrm{d}\omega \end{aligned} \tag{13}$$

where $\hat{s}(\vec{\boldsymbol{k}}, \omega)$ is the FT of $s(\vec{\boldsymbol{x}}, t)$, as defined in (2), and the transformed wavelet in the wave-number frequency domain is defined as follows:

$$\hat{\psi}_{a,c,\theta;\vec{\boldsymbol{b}},\tau}(\vec{\boldsymbol{k}}, \omega) = a^{3/2} \hat{\psi}\left(ac^{1/3}\boldsymbol{r}_{-\theta} \cdot (\vec{\boldsymbol{k}}), ac^{-2/3}\omega\right) \times \exp\left(-\mathrm{i}\left(\vec{\boldsymbol{k}} \cdot \vec{\boldsymbol{b}} + \omega\tau\right)\right). \tag{14}$$

In this process, the chosen mother wavelet $\hat{\psi}$ in the spatiotemporal domain is converted into a transformed wavelet $\hat{\psi}_{a,c,\theta;\vec{\boldsymbol{b}},\tau}$ in the wave-number frequency domain by scaling a, shifting τ in time and $\vec{\boldsymbol{b}}$ in space, rotating θ, and speed tuning c to "match" a particular wave component $\hat{s}(\vec{\boldsymbol{k}}_p, \omega_p)$ of the signal.

To better explain the results obtained from image processing by the STCWT technique, we must interpret several basic properties in detail. Equation (14) shows that the wave number can be transformed from $\vec{\boldsymbol{k}}$ into $ac^{1/3}\boldsymbol{r}_{-\theta}(\vec{\boldsymbol{k}})$, and the frequency can be transformed from ω into $ac^{-2/3}\omega$ after scaling, speed tuning, and rotating a wavelet. As shown in (12), ω_0 and $\vec{\boldsymbol{k}}_0$ are the frequency and wave number, respectively, at which the peak

energy of the mother Morlet function occurs in Fourier space. After transformation, the new peak energy of the transformed Morlet wavelet is converted to a particular position $(\vec{\boldsymbol{k}}_p, \omega_p)$, which is defined as follows:

$$ac^{1/3}\boldsymbol{r}_{-\theta} \cdot (\vec{\boldsymbol{k}}_p) = \vec{\boldsymbol{k}}_0 \tag{15}$$

$$ac^{-2/3}\omega_p = \omega_0. \tag{16}$$

Therefore, we could derive the STCWT frequency spectra $S(\vec{\boldsymbol{k}}, \omega)$ [instead of the 6-D representation $S(a, c, \theta; \vec{\boldsymbol{b}}, \tau)$] of the signal $s(\vec{\boldsymbol{x}}, t)$ for each specific position of interest $\vec{\boldsymbol{x}}$ at any instant t by employing the relations defined in (15) and (16).

B. Wave Group Velocity Estimation From STCWT

Here, we discuss the relationship between the STCWT results and the ocean wave parameters. Before estimating the wave group velocity, we must obtain the wave phase speed information that describes the propagation speed of the surface wave profile. The wave phase speed $\vec{\boldsymbol{v}}_p$ and the wave group velocity C_g are derived from the frequency, wave number, and water depth h, as follows:

$$\vec{\boldsymbol{v}}_p = \frac{\omega}{\vec{\boldsymbol{k}}} \tag{17}$$

$$C_g = \frac{1}{2}\left(1 + \frac{2kh}{\sinh(2kh)}\right)|\vec{\boldsymbol{v}}_p|. \tag{18}$$

Because (13) is a representation with six parameters that are directly associated with motion features, we can develop the velocity relationship by combining (15) and (16) to produce

$$\frac{\omega_p}{\vec{\boldsymbol{k}}_p} = c\boldsymbol{r}_{-\theta} \cdot \left(\frac{\omega_0}{\vec{\boldsymbol{k}}_0}\right) \longrightarrow \vec{\boldsymbol{v}}_p = c\boldsymbol{r}_{-\theta} \cdot \vec{\boldsymbol{v}}_0 \tag{19}$$

$$\begin{aligned} C_g &= \frac{1}{2}\left(1 + \frac{2kh}{\sinh(2kh)}\right)|\vec{\boldsymbol{v}}_p| \\ &= \frac{1}{2}\left(1 + \frac{2kh}{\sinh(2kh)}\right)|c\boldsymbol{r}_{-\theta} \cdot \vec{\boldsymbol{v}}_0|. \end{aligned} \tag{20}$$

This representation means that the wave phase speed $\vec{\boldsymbol{v}}_p$ of a particular wave component of interest can be estimated by mapping the original velocity plane of mother wavelet moving with velocity $\vec{\boldsymbol{v}}_0$; this mapping can be accomplished by an orientation change θ and a proportional change c in its velocity magnitude. The speed-tuning parameter c is a scaling operator to change the velocity plane of the mother wavelet to a new velocity plane associated with the wave component of interest.

Equations (19) and (20) present the continuous functions, but the sea-surface image sequences that are discussed in most applications consist of discrete data. To analyze these digital wave image signals by the theory of STCWT, it is necessary to sample the wavelet function. Jordan and Miksad [19] have presented a method to sample a 1-D wavelet function for time series analysis. Because our study focuses on the issue of spatiotemporal signals, we must discuss methods to sample higher dimensional wavelet functions.

As shown in Fig. 1, a physical spatial series has sampling space Δx and a total number of sample points N_x. The total nondimensional space length is $2X$, which is mapped for N_x points. The relationship between the dimensional and nondimensional sampling spaces can be obtained from the number of sample points of the wavelet function as follows:

$$[-X, X] \leftrightarrow [0, N_x\Delta x]. \tag{21}$$

Similarly, $2T$ is the total nondimensional length of the wavelet function in the time domain, and $N_t\Delta t$ is the total number of elements in the dimensional time domain

$$[-T, T] \leftrightarrow [0, N_t\Delta t]. \tag{22}$$

Equation (19) can be written as follows:

$$\vec{\boldsymbol{v}}_p = c\boldsymbol{r}_{-\theta} \cdot \vec{\boldsymbol{v}}_0 \frac{TN_x\Delta x}{XN_t\Delta t}. \tag{23}$$

As shown in (11) and (12), $T = X$ under the assumption that $\varepsilon = 1$. Then, (23) can be simplified as follows:

$$\vec{\boldsymbol{v}}_p = c\boldsymbol{r}_{-\theta} \cdot \vec{\boldsymbol{v}}_0 \frac{N_x\Delta x}{N_t\Delta t} \tag{24}$$

and the wave group velocity C_g can be written as following the discrete type

$$C_g = \frac{1}{2}\left(1 + \frac{2kh}{\sinh(2kh)}\right)\left(|c\boldsymbol{r}_{-\theta} \cdot \vec{\boldsymbol{v}}_0|\frac{N_x\Delta x}{N_t\Delta t}\right). \tag{25}$$

III. Verification by Simulated Sea-Surface Image Sequences

For the sake of verifying the practicability of wave group velocity estimation by the STCWT, different simulated sea-surface image sequences were applied in our study. The simulation methods and analysis results are shown here.

A. Regular Wave Image Simulation and Analysis

For the primary test, simplified regular wave image sequences were simulated. Single direction regular waves that propagate in the time–space domain were generated by

$$\eta(t, x, y) = A\cos[k(x\cos\alpha + y\sin\alpha) - \omega t] \tag{26}$$

in which A is the amplitude of the wave component, k is the wave number, ω is the angular frequency, and α is the incident wave direction. Equation (26) describes the monoharmonic waves in the spatiotemporal domain. Under the assumption of linear waves, the input wave-number value is calculated by the dispersion relationship, which describes the relationship between the angular frequency ω, the wave number k, and the water depth h

$$\omega = \sqrt{gk\tanh(kh)}. \tag{27}$$

The phenomena of wave shoaling, refraction, and reflection that control the 3-D transformation of waves as they approach the shore are considered in the simulation of our study. The equations for simulating sea-surface waves that are influenced

by reflection, refraction, and shoaling are shown as follows [20]–[22]:

$$\eta(t,x,y) = A_i[(\cos(P+\varepsilon_i) + K_R\cos(P+\varepsilon_i+\varepsilon_r))\cos(\omega t) + (\sin(P+\varepsilon_i)+K_R\sin(P+\varepsilon_i+\varepsilon_r))\sin(\omega t)] \tag{28}$$

$$A_i = A_0 K_s \tag{29}$$

$$K_s(x,y) = \left[\tanh(kh(x,y)) + \frac{kh(x,y)}{\cosh^2(kh(x,y))}\right]^{-0.5} \tag{30}$$

$$P = \int_0^x (k\cos\theta)\,dx + ky\sin\theta. \tag{31}$$

The parameters k and α were defined in (26), K_s is the shoaling coefficient, K_R is the reflection coefficient, ε_i is the phase of the incident waves, ε_r is the phase of the reflected waves, A_i is the amplitude of the incident waves, and $h(x,y)$ describes the bathymetry conditions in the space domain. For the initial conditions of the regular wave case, a height of 1 m, a direction of 135°, and a period of 7 s were used. We assumed that there is a structure at the north edge of the wave field that induces a reflection coefficient of $K_R = 0.5$. Because we are analyzing digital images, the sampling parameters of the digital images must be determined. In our study, the spatial resolution of the image is 5 m/pixel, and the size of the image is 128 pixels × 128 pixels.

The simulated waves and the corresponding bathymetry are shown in Fig. 2. For the time domain of the wave image sequences, the time resolution of the wave image sequences is 1 s. The surface image sequences in the time domain all contain 128 continuous images. Based on (13), the result of the wave analysis by STCWT is $S(\vec{\boldsymbol{b}}, \tau, \theta; a, c)$, which can be transformed into a spectrum $S(\vec{\boldsymbol{x}}, t; \omega, k, \theta)$ by (15) and (16). $S(\vec{\boldsymbol{x}}, t; \omega, k, \theta)$ represents the spectrum in the spatiotemporal domain. The spectrum function $S(\omega, k, \theta)$ represents the distribution of the wave energy in the frequency and wave-number domains. To represent these 3-D results, we integrate the function $S(\omega, k, \theta)$ over the frequency and direction domains to obtain $S(k, \theta)$ and $S(\omega, k)$, respectively. Fig. 3 shows $S(k, \theta)$ and $S(\omega, k)$ from different locations in Fig. 2. As shown in Fig. 2, three different locations with different bathymetry conditions were selected for identification of the spectral features from the inhomogeneous sea surface.

Based on the linear wave theory, the wave number and the wave direction should change as the water depth in the shallow-water area changes because of wave shoaling and wave refraction. The wave frequency, however, should be constant during wave propagation. The left-hand side of Fig. 3 shows that the energy distribution of $S(k, \theta)$ moves from low wave number to high wave number as the water depth decreases. The energy distribution of the direction domain is also influenced by different locations as a result of wave refraction. The right-hand side of Fig. 3 presents the $S(\omega, k)$ results from different locations. Unlike the energy distribution in the wave-number domain, the energy distribution in the frequency domain is constant. The two energy density groups in each spectrum represent the energy from the incident and reflected waves.

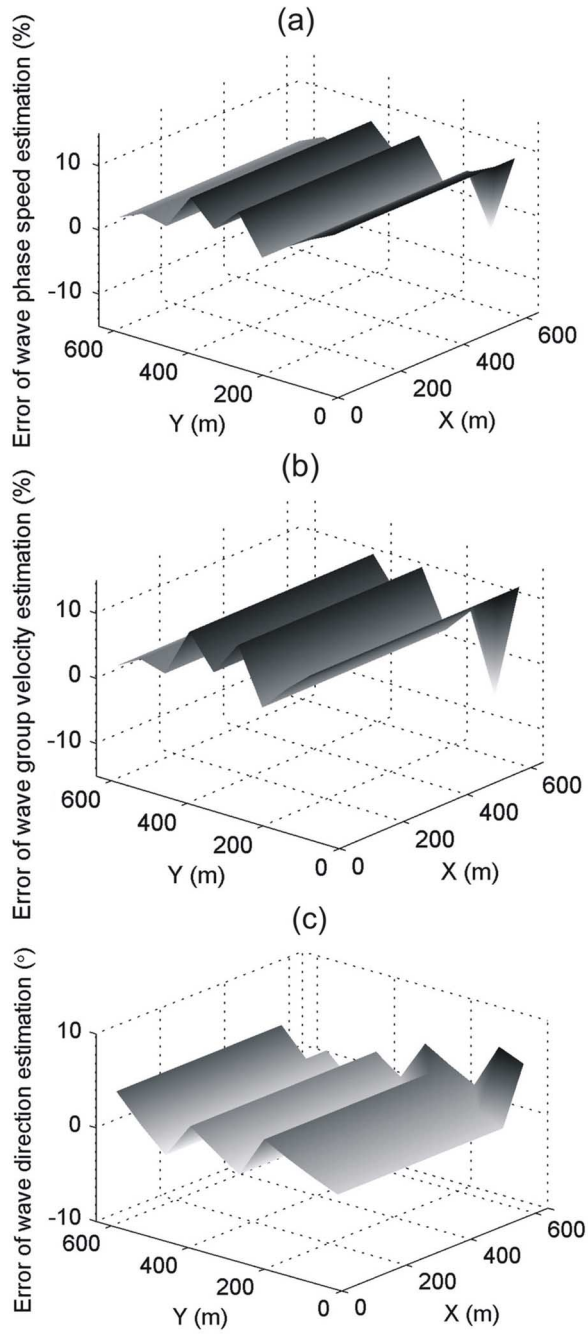

Fig. 5. (a) Wave phase speed accuracies; (b) wave group velocity accuracies; and (c) wave direction accuracies from different locations on the inhomogeneous wave image by wavelet transform.

The right-hand side of Fig. 3 presents the spectra in the wave number and frequency domains. We also present the theoretical dispersion relation curves corresponding to different bathymetry conditions. We observed that the energy from every $S(\omega, k)$ was consistent with the corresponding dispersion relation curve, which means that the relationship between ω and k from the wavelet results was consistent with that of the linear wave dispersion theory.

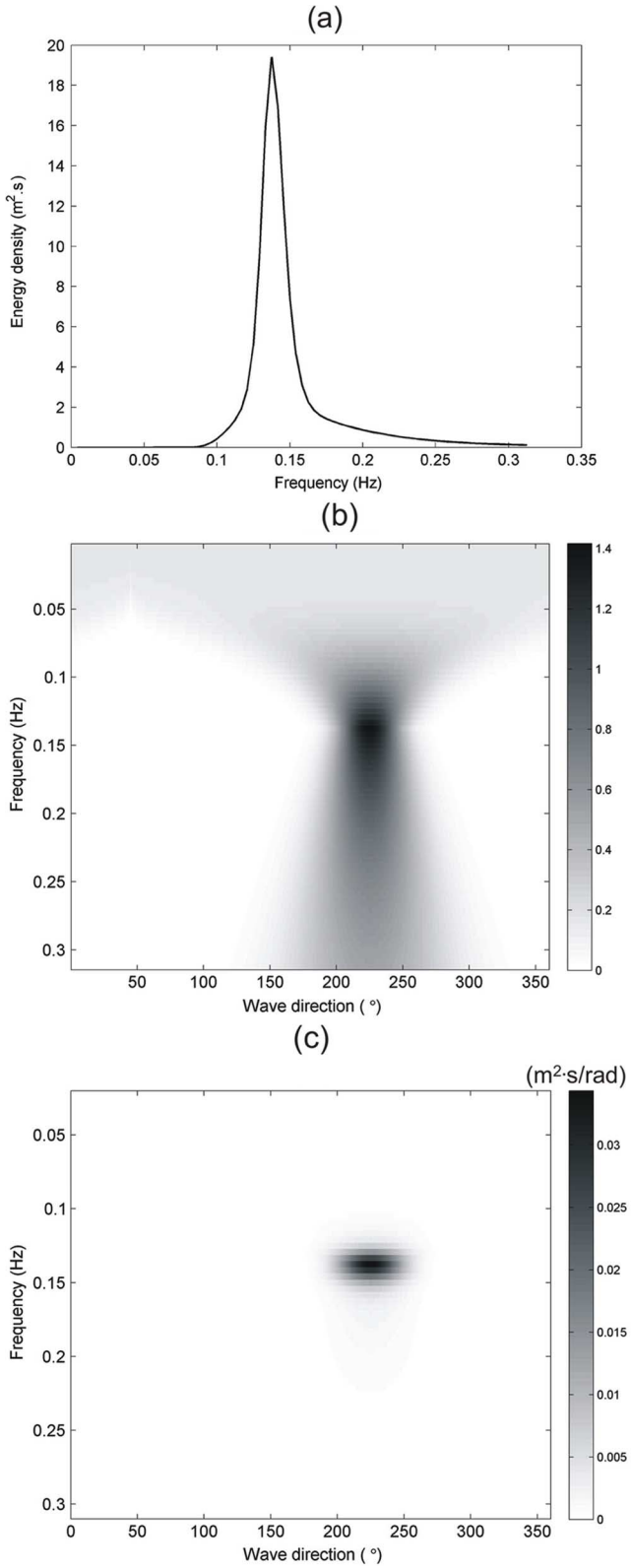

Fig. 6. (a) 1-D wave spectrum. (b) Spreading function. (c) Directional wave spectrum for simulating irregular wave image.

Fig. 4 presents the wave group velocity estimation results from the entire inhomogeneous sea-surface image. The arrows on the image indicate the wave group velocity and wave direction results estimated by the STCWT. To verify the accuracy of our results, we calculated the deviations between the simulated parameters and the results from the STCWT.

Fig. 5 presents the accuracy of the wave phase speed, the wave group velocity, and the wave direction from the entire sea surface. The accuracies of these three subplots are more stable along the x-axis than along the y-axis. The variant bathymetry causes the varying accuracies along the y-axis. In addition, the maximum difference between the simulated and estimated wave group velocity values was approximately 10% in this case. The errors of the estimated wave direction were all less than 10°. We noticed that the accuracy of the wave group velocity results was poorer than that of the wave phase speed results. Based on (18), the wave group velocity is derived from the wave number k, the water depth h, and the wave phase speed $\vec{\boldsymbol{v}}_p$. To increase the accuracy of the wave group velocity, the accuracies of k, h and $\vec{\boldsymbol{v}}_p$ must be improved. Wu *et al.* [18], [23] also proved that the image resolution and wave image size are critical to improvement of the estimated wave parameters.

B. Irregular Wave Simulation and Analysis

The STCWT presents reasonable results for the estimation of wave parameters in the case of regular waves. However, real ocean waves in nature are always irregular. In addition to the case of regular waves, we also discuss wave group velocity estimations for the irregular wave case by STCWT. The irregular wave simulation is based on the wave spectrum $S(f)$. Considering the propagation of waves in shallow water, the TMA spectrum $S(f)$ was applied here. The TMA spectrum is intended for used in water of finite depth [24] and is derived from the JOint North Sea WAve Project (JONSWAP) spectrum $S_j(f)$. The name TMA derives from the names of the data sets Texel, Marsen, and Arsloe [25]. These equations are described as follows:

$$S(f) = \phi S_j(f) \tag{32}$$

$$\phi = \frac{\tanh^2(kh)}{1 + ((2kh)/\sinh(2kh))} \tag{33}$$

$$S_j(f) = \beta_j H_{1/3}^2 T_p^{-4} f^{-5} \times \exp\left(-1.25(T_p f)^{-4}\right) \gamma^{\exp[-(f/f_p - 1)^2/2\sigma^2]} \tag{34}$$

$$f_p = 1/T_p \tag{35}$$

$$\sigma = \begin{cases} 0.07, & f \le f_p \\ 0.09, & f > f_p \end{cases} \tag{36}$$

$$\beta_j = \frac{0.0624}{0.230 + 0.0336\gamma - 0.185(1.9 + \gamma)^{-1}} \times [1.094 - 0.01915 \ln \gamma]. \tag{37}$$

As shown in (32) and (33), ϕ is a function to modify the JONSWAP spectrum to adjust the spectral features in the shallow-water area. From (34)–(37), T_p is the peak wave period, and f_p is the peak wave frequency. Goda [26] reported that the value of γ is within the range from 1 to 20, and $\gamma = 9$ in this study. Because of the multidirectional nature of ocean waves, a Mitsuyasu-type directional spreading function $G(f, \theta)$ was used [26]

$$S(f, \theta) = S(f) G(f, \theta) \tag{38}$$

$$G(f, \theta) = G_0 \cos^{2s}((\theta - \theta_p)/2) \tag{39}$$

$$\int_{-\pi}^{\pi} G(f,\theta)\,\mathrm{d}\theta = 1 \tag{40}$$

$$G_0 = \frac{1}{\pi}2^{2s-1}\frac{\Gamma^2(s+1)}{\Gamma(2s+1)} \tag{41}$$

$$s = \begin{cases} s_{\max}(f/f_p)^5, & f \le f_p \\ s_{\max}(f/f_p)^{-2.5}, & f > f_p \end{cases} \tag{42}$$

$$\begin{aligned} &s_{\max} = 10 \quad \text{wind waves} \\ &s_{\max} = 25 \quad \text{swell with short decay distance} \\ &s_{\max} = 75 \quad \text{swell with long decay distance.} \end{aligned} \tag{43}$$

In (39), θ_p is the dominant wave direction. The parameter s controls the angular distribution of the waves and is known to vary with the frequency. The spreading parameter $s_{\max}$ changes with different wave cases. In our paper, $s_{\max}$ is set equal to 10, which describes the case of wind waves. The relationship between the amplitude of the waves (A) and the directional spectrum is shown in

$$\sum_{\omega}^{\omega+\mathrm{d}\omega}\sum_{\theta}^{\theta+\mathrm{d}\theta} S(\omega,\theta)\Delta\omega\Delta\theta = \frac{1}{2}A^2. \tag{44}$$

For the continuous frequency function, the distributions of both the wave frequency and the wave number should be from $-\infty \sim \infty$. However, the wave image signals are composed of discrete data. We have divided the frequency and wave number into n parts, and the direction was divided into m parts

$$\omega_n = n\omega_i \tag{45}$$

$$k_{mn_x} = k_n\cos\theta_m = nk_i\cos\theta_m \tag{46}$$

$$k_{mn_y} = k_n\sin\theta_m = nk_i\sin\theta_m. \tag{47}$$

In (45)–(47), ω_i and k_i are the initial conditions of the frequency and wave number, respectively. Considering negative wave frequencies, the discrete amplitude of the waves (A_n) is expressed as follows:

$$A_n = \sum_{n=-N/2}^{N/2}\sum_{m=1}^{M}\sqrt{S(\omega_n,\theta_m)\Delta\omega\Delta\theta}. \tag{48}$$

The discrete wave function is shown in

$$\begin{aligned} &\eta(t,x,y) \\ &\quad = \sum_{n=-N/2}^{N/2}\sum_{m=1}^{M}\sqrt{S(\omega_n,\theta_m)\Delta\omega\Delta\theta} \\ &\qquad \times\left(\cos\left(n\omega t - k_{mn_x}x - k_{mn_y}y - \varepsilon_{mn}\right)\right). \end{aligned} \tag{49}$$

To speed up the wave image sequence simulation, the fast FT was applied here [11]. We added the imaginary part of the wave components into (49) and derived it by the character of the trigonometric functions

$$\begin{aligned} &\sum_{n=-N/2}^{N/2}\sum_{m=1}^{M}\sqrt{S(\omega_n,\theta_m)\Delta\omega\Delta\theta} \\ &\quad\times\left[\cos\left(n\omega t - k_{mn_x}x - k_{mn_y}y - \varepsilon_{mn}\right)\right. \\ &\qquad \left.+\mathrm{i}\sin\left(n\omega t - k_{mn_x}x - k_{mn_y}y - \varepsilon_{mn}\right)\right] \\ &\quad = \sum_{n=-N/2}^{N/2}\sum_{m=1}^{M}\left[\sqrt{S(\omega_n,\theta_m)\Delta\omega\Delta\theta}\right. \\ &\qquad \times\left(\cos\left(k_{mn_x}x + k_{mn_y}y + \varepsilon_{mn}\right)\right. \\ &\qquad\quad \left.\left.-\mathrm{i}\sin\left(k_{mn_x}x + k_{mn_y}y + \varepsilon_{mn}\right)\right)\right. \\ &\qquad \left.\times\exp(\mathrm{i}n\omega t)\right] \\ &\quad = \sum_{n=-N/2}^{N/2}(a_n - \mathrm{i}b_n)\exp(\mathrm{i}n\omega t) \end{aligned} \tag{50}$$

$$\begin{aligned} a_n = &\sum_{m=1}^{M}\sqrt{S(\omega_n,\theta_m)\Delta\omega\Delta\theta} \\ &\times\cos(k_n(x\cos\theta_m + y\sin\theta_m) + \varepsilon_{mn}) \end{aligned} \tag{51}$$

$$\begin{aligned} b_n = &\sum_{m=1}^{M}\sqrt{S(\omega_n,\theta_m)\Delta\omega\Delta\theta} \\ &\times\sin(k_n(x\cos\theta_m + y\sin\theta_m) + \varepsilon_{mn}). \end{aligned} \tag{52}$$

Now, (50) can be presented as the inverse fast Fourier transform (IFFT) of the function $(a_n - \mathrm{i}b_n)$, and we can simulate the irregular wave image sequences by the fast FT algorithm

$$\sum_{n=-N/2}^{N/2}(a_n - \mathrm{i}b_n)\exp(\mathrm{i}n\omega t) = \mathrm{IFFT}(a_n - \mathrm{i}b_n). \tag{53}$$

Equation (49) differs from to (53); 3-D data are calculated in (49) to simulate wave image sequences, but only 2-D data are calculated in (53). The simulation proceeds faster by (53) than by (49). This paper simulates the irregular wave image sequences by the aforementioned methods. The directional spectrum that is the input for (49) and (53) is shown in Fig. 6. Initial wave conditions with a 1.5-m significant wave height, 225° dominant wave direction, and 7-s mean wave period were simulated. The simulated irregular wave image is shown in Fig. 7.

The wave spectra $S(k,\theta)$ and $S(\omega,k)$ from different locations of the irregular wave image are shown in Fig. 8. The energy peak of $S(k,\theta)$ moves to high wave number gradually as the analysis location moves to shallower water. Compared with the analyzed results from the regular wave case, the $S(k,\theta)$ analyzed from the irregular wave case exhibits a slightly scattered energy distribution. Because of the superposition of different wave components with random phases, the spectra from the irregular waves are more random and scattered than the spectra from regular waves. Similarly to $S(k,\theta)$ in Fig. 3, the energy distribution from each $S(\omega,k)$ is also consistent with its dispersion relation curve.

The estimated wave group velocities at different locations are presented in Fig. 7. Fig. 9 shows the differences between the simulated parameters and the estimated values of the various wave parameters. The results show that the differences between the irregular cases are more evident than those between the regular wave cases. However, these larger differences in the irregular wave cases do not imply poor estimation accuracy. As we mentioned above, the irregular waves are superposed by different wave components with random phases. This superposition produces higher variability of the wave features from the irregular waves. From the results in Fig. 9, we also observed

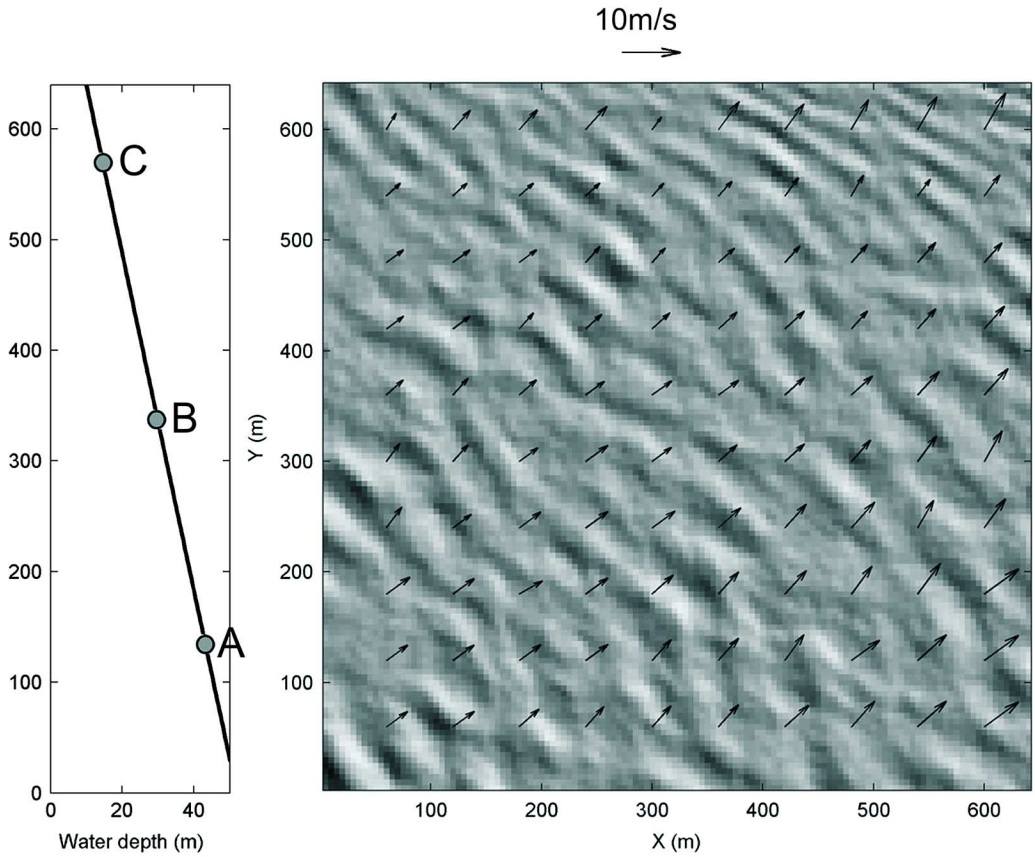

Fig. 7. Simulated irregular wave image and its corresponding bathymetry. The arrows on the wave image represent the wave group velocity and direction results estimated by STCWT.

that the differences between the simulated parameters and the estimated values are obvious at the locations near the edges of the sea-surface images. This visible difference is the impact of the image edges, which is related to the leakage of the wavelet transform [5].

IV. Discussion

In addition to our studies, a large number of other studies have assessed the predominance of wavelet theory in different applications. No matter what types of data are analyzed, it is necessary to identify the capability of nonstationary and inhomogeneous signal analysis in different situations. Because our study analyzed the spatiotemporal sea-surface image sequences, we need to determine the ranges of the wave field analyzed by the wavelet functions under different wave conditions. The analyzed range of the wave field is called the width of the window function by some authors [27]. It is related to the nearly nonzero part of the wavelet function. The wavelet window width implies the stationary and homogeneous range inside the entire wave image. Based on the features of the wavelet functions, the wavelet method does not require the preselection of a window width and does not have a fixed time–frequency window over the time–frequency space. The time and space window widths in the time and space domains can be defined by the standard deviation (σ_t and σ_x) of the mother wavelet function [19]

$$\sigma_t = \left(\int_{-\infty}^{\infty} \left(t - \left(\frac{\int_{-\infty}^{\infty} t|\psi(t)|^2 \,\mathrm{d}t}{\int_{-\infty}^{\infty} |\psi(t)|^2 \,\mathrm{d}t} \right) \right)^2 |\psi(t)|^2 \,\mathrm{d}t \right)^{0.5} \tag{54}$$

$$\sigma_x = \left(\int_{-\infty}^{\infty} \left(x - \left(\frac{\int_{-\infty}^{\infty} x|\psi(x)|^2 \,\mathrm{d}x}{\int_{-\infty}^{\infty} |\psi(x)|^2 \,\mathrm{d}x} \right) \right)^2 |\psi(x)|^2 \,\mathrm{d}x \right)^{0.5} \tag{55}$$

in which $\psi(t)$ and $\psi(x)$ are the mother wavelet function in the time and space domains. The wavelet window widths in the frequency and wave-number domains can be defined by the standard deviations (σ_ω and σ_{k_x}) of the mother wavelet function in the frequency domains

$$\sigma_\omega = \left(\int_{-\infty}^{\infty} \left(\omega - \frac{\int_{-\infty}^{\infty} \omega|\hat{\psi}(\omega)|^2 \,\mathrm{d}\omega}{\int_{-\infty}^{\infty} |\hat{\psi}(\omega)|^2 \,\mathrm{d}\omega} \right)^2 |\hat{\psi}(\omega)|^2 \,\mathrm{d}\omega \right)^{0.5} \tag{56}$$

$$\sigma_{k_x} = \left(\int_{-\infty}^{\infty} \left(k_x - \frac{\int_{-\infty}^{\infty} k_x|\hat{\psi}(k_x)|^2 \,\mathrm{d}k_x}{\int_{-\infty}^{\infty} |\hat{\psi}(k_x)|^2 \,\mathrm{d}k_x} \right)^2 |\hat{\psi}(k_x)|^2 \,\mathrm{d}k_x \right)^{0.5}. \tag{57}$$

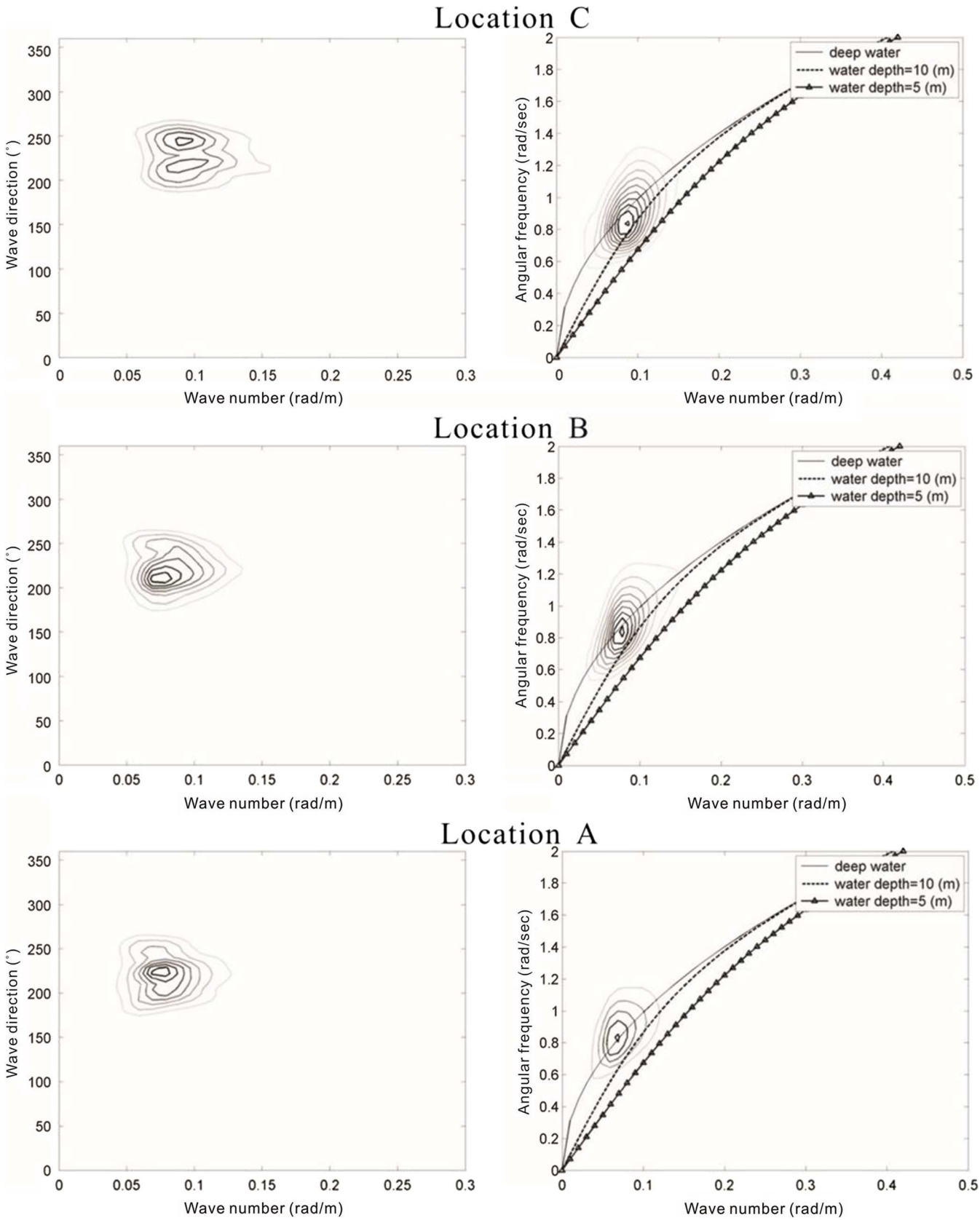

Fig. 8. The wave spectra $S(k,\theta)$ and $S(\omega,k)$ from different locations of irregular and inhomogeneous wave image sequences.

Our previous study [18] has revealed that the wavelet window widths are approximately seven times the standard deviations of the mother wavelet functions in the different domains. The different transformed wavelet functions imply different window widths. To analyze the different wave components in the entire sea-surface image, different wavelet functions from the mother

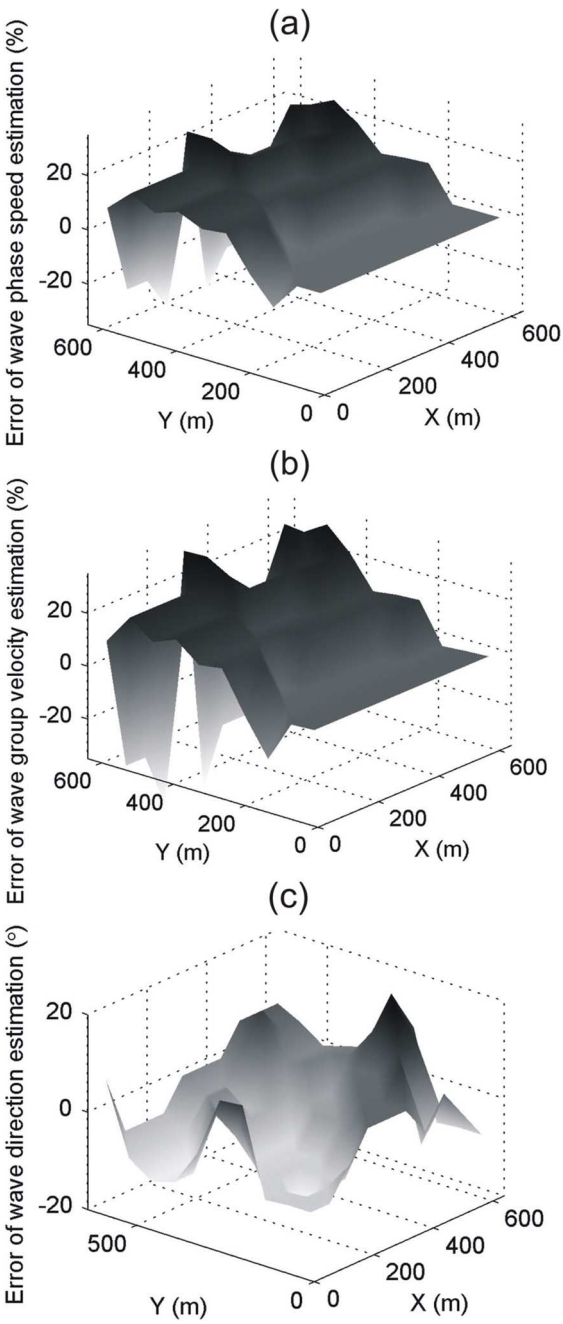

Fig. 9. (a) Wave phase speed accuracies; (b) wave group velocity accuracies; and (c) wave direction accuracies from different locations of inhomogeneous wave image sequences by STCWT.

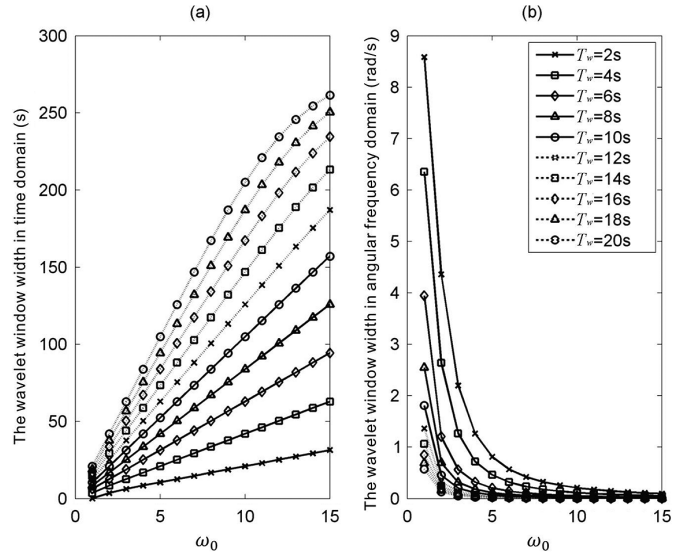

Fig. 10. Wavelet window widths in (a) time and (b) frequency domains under different ocean wave period conditions (T_w).

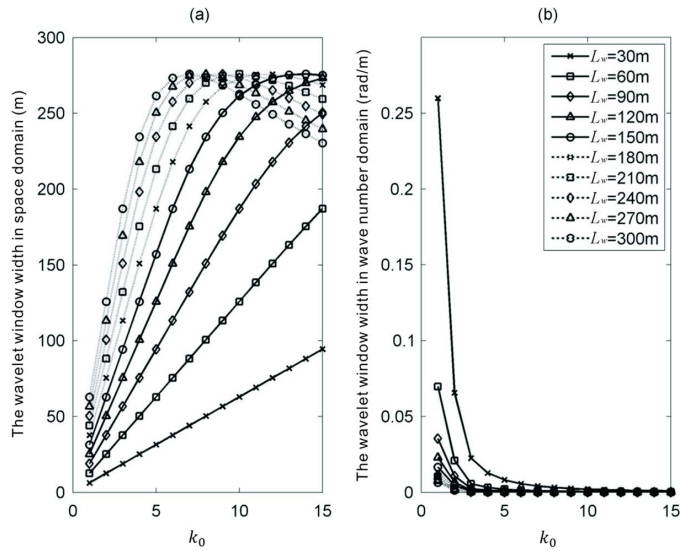

Fig. 11. Analyzed ranges in (a) space and (b) wave-number domains under different ocean wavelength conditions (L_w).

wavelet with different parameters are used. Figs. 10 and 11 present the window widths in different domains for different wave analysis cases. Because the wave image analysis is discrete, the wave image sequence number, image size, time resolution, and space resolution are all factors that determine the wavelet window width. This paper uses the same image parameters conditions as those used to simulate the wave field in Section III.

As shown in Fig. 10, the wavelet function provides a wider window in the time domain for the long wave period case, and the wavelet function in the frequency domain is a narrow band spectrum. Similar to the results of Fig. 10, Fig. 11 shows the window widths in the space and wave-number domains. To analyze the long wavelength case, the wavelet function provides a wider window in the space domain. In addition, ω_0 and $\vec{\boldsymbol{k}}_0$ are the key parameters to change the window width of the wavelet function. To analyze highly nonstationary or inhomogeneous wave image sequences, lower values of ω_0 or $\vec{\boldsymbol{k}}_0$ are suggested. However, higher values of ω_0 and $\vec{\boldsymbol{k}}_0$ are necessary to obtain high-resolution results in the frequency domain. To estimate the wave parameters accurately, different values of ω_0 and $\vec{\boldsymbol{k}}_0$ in the mother wavelet functions must be considered for different wave situations. By observing cases of long wave periods, we have observed that the relationship between ω_0 and the wavelet window width in the time domain is not linear. A similar phenomenon is also observed in the case of Fig. 11(a). This result is caused by the limited sizes of the image sequences. Figs. 10

and 11 are estimated from the 128 pixel $\times$ 128 pixel sizes in the space domain and the 128 continuous image sequences in the time domain. This size is inadequate for the longer wave cases. To obtain accurate results from these cases, it is necessary to enlarge the size of image sequences in both time and space domains.

V. Conclusion

The wave group velocity is critical to the discussion of the mechanics of ocean waves and the rate of wave energy motion. It is possible to estimate this parameter from the spatiotemporal sea-surface features by an applicable spectral transformation. To extract the spatial information from the inhomogeneous sea surface, this paper attempts to apply the theory of the STCWT to estimate the wave group velocities and discuss their accuracies. The achievement of this study is useful for understanding the wave mechanics of inhomogeneous water areas.

Because the original STCWT theory was not used for wave group velocity estimation from sea-surface image sequences, our study has developed an algorithm to derive the wave group velocity of ocean waves from the STCWT and linear wave theory. To verify its correctness and practicability, different kinds of simulated sea-surface image sequences were analyzed by the STCWT. The detailed algorithms used to simulate regular and irregular sea-surface image sequences were presented in our paper. Because of the superposition of different wave components with random phases, the accuracy of the simulated parameters and estimated values in the regular case were higher than the accuracy of the parameters and values from the irregular wave case. However, the spectral results from the different simulated wave cases confirm that the energy distribution was consistent with the linear wave theory, which we used in the irregular wave simulation.

To determine the applicability of the STCWT algorithm to inhomogeneous wave analysis, this paper also discusses the analyzed ranges (wavelet window widths) of the wave field under different wave conditions. It should be noted that the image sequence number, image size, time resolution, space resolution, and ω_0 and $\vec{k}_0$ parameters are all factors that influence the results of the wavelet analysis. After the study and discussion of these cases, we can conclude that the analysis of inhomogeneous sea-surface image sequences by the STCWT is feasible.

Acknowledgment

The authors would like to thank the referees for helpful comments and suggestions.

References

[1] W. J. Pierson, *Practical Methods for Observing and Forecasting Ocean Waves by Means of Wave Spectra and Statistics*. Washington, DC, USA: Hydrographic Office, 1955, ch. 2.

[2] S. R. Massel, "Wavelet analysis for processing of ocean surface wave records," *Ocean Eng.*, vol. 28, pp. 957–987, 2001.

[3] H. S. Lee and S. H. Kwon, "Wave profile measurement by wavelet transform," *Ocean Eng.*, vol. 30, pp. 2313–2328, 2003.

[4] G. E. Carlson, "Wavelet processing of SAR ocean wave images," in *Proc. Int. Geosci. Remote Sens. Symp.*, 1995, pp. 679–681.

[5] L. Z.-H. Chuang, L.-C. Wu, D.-J. Doong, and C. C. Kao, "Two-dimensional continuous wavelet transform of simulated spatial images of waves on a slowly varying topography," *Ocean Eng.*, vol. 35, pp. 1039–1051, 2008.

[6] R. Murenzi, "Wavelet transforms associated to the n-dimensional euclidean group with dilations: Signal in more than one dimension," in *Wavelets*, J.-M. Combes, A. Grossmann, and P. Tchamitchian, Eds. Berlin, Germany: Springer-Verlag, 1989, pp. 239–246.

[7] M. Duval-Destin and R. Murenzi, "Spatio-temporal wavelets: Application to the analysis of moving patterns," in *Progress in Wavelet Analysis and Applications*, Y. Meyer and S. Roques, Eds. Gif-sur-Yvette, France: Editions Frontieres, 1993, pp. 399–408.

[8] J. P. Leduc, "Spatio-temporal wavelet transforms for digital signal analysis," *Signal Process.*, vol. 60, pp. 23–41, 1997.

[9] I. R. Young, W. Rosenthal, and F. Ziemer, "A three-dimensional analysis of marine radar images for the determination of ocean wave directionality and surface currents," *J. Geophys. Res., Oceans*, vol. 90, pp. 1049–1059, 1985.

[10] J. M. Wanek and C. H. Wu, "Automated trinocular stereo imaging system for three-dimensional surface wave measurements," *Ocean Eng.*, vol. 33, pp. 723–747, 2006.

[11] R. G. Dean and R. A. Dalrymple, *Water Wave Mechanics for Engineers & Scientists*. Singapore: World Scientific, 1991, ch. 4.

[12] D. Reeve, A. J. Chadwick, and C. A. Fleming, *Coastal Engineering: Process, Theory and Design Practice*. Oxon, U.K.: Spon, 2004, ch. 2.

[13] F. A. Mujica, "Spatio-temporal continuous wavelet transform for motion estimation," Ph.D. dissertation, Electr. Comput. Eng. Dept., Georgia Inst. Technol., Atlanta, GA, USA, 1999.

[14] F. A. Mujica, J. P. Leduc, R. Murenzi, and M. J. T. Smith, "A new motion parameter estimation algorithm based on the continuous wavelet transform," *IEEE Trans. Image Process.*, vol. 9, no. 5, pp. 873–888, May 2000.

[15] J. P. Antoine, *2-Dimensional Wavelets and Their Relatives*. Cambridge, U.K.: Cambridge Univ. Press, 2004, ch. 10.

[16] D. Barache, J. P. Antoine, and J. M. Dereppe, "The continuous wavelet transform, an analysis tool for NMR spectroscopy," *J. Magn. Resonan.*, vol. 128, pp. 1–11, 1997.

[17] M. C. Huang, "Wave parameters and functions in wavelet analysis," *Ocean Eng.*, vol. 31, pp. 111–125, 2004.

[18] L.-C. Wu, L. Z.-H. Chuang, D.-J. Doong, and C. C. Kao, "Ocean remotely sensed image analysis using two-dimensional continuous wavelet transforms," *Int. J. Remote Sens.*, vol. 32, pp. 8779–8798, 2011.

[19] D. Jordan, R. W. Miksad, and E. J. Powers, "Implementation of the continuous wavelet transform for digital time series analysis," *Rev. Sci. Instrum.*, vol. 68, pp. 1484–1494, 1997.

[20] H. K. Chang and T. W. Hsu, "A two-point method for estimating wave reflection over a sloping beach," *Ocean Eng.*, vol. 30, pp. 1833–1847, 2003.

[21] C. Hsien-Kuo, "A three-point method for separating incident and reflected waves over a sloping bed," *China Ocean Eng.*, vol. 16, p. 13, 2002.

[22] K. Horikawa, *Nearshore Dynamics and Coastal Processes: Theory, Measurement, and Predictive Models*. Tokyo, Japan: Univ. Tokyo Press, 1988, ch. 3, pt. I, pp. 49–78.

[23] L.-C. Wu, L. Z.-H. Chuang, D.-J. Doong, and C. C. Kao, "Quantification of non-homogeneity from ocean remote-sensing images using two-dimensional continuous wavelet transforms," *Int. J. Remote Sens.*, vol. 32, pp. 1303–1318, 2011.

[24] E. Bouws, H. Günther, W. Rosenthal, and C. L. Vincent, "Similarity of the wind wave spectrum in finite depth water: 1. Spectral form," *J. Geophys. Res., Oceans*, vol. 90, pp. 975–986, 1985.

[25] L. H. Holthuijsen, *Waves in Oceanic and Coastal Waters*. Cambridge, U.K.: Cambridge Univ. Press, 2007, ch. 8.

[26] Y. Goda, "A comparative review on the functional forms of directional wave spectrum," *Coast. Eng. J.*, vol. 41, pp. 1–20, 1999.

[27] C. K. Chui, *An Introduction to Wavelets*. New York, NY, USA: Academic, 1992, ch. 1.

Laurence Zsu-Hsin Chuang received the B.E. degree in civil engineering from the National Cheng Kung University, Tainan, Taiwan, in 1984, the M.S. degree in civil engineering from Colorado State University, Boulder, CO, USA, in 1988, and the Ph.D. degree in civil engineering from North Carolina State University, Raleigh, NC, USA, in 1992.

He was a Researcher at Tainan Hydraulics Laboratory, Tainan, Taiwan, from 1992 to 1998 and the Deputy Director of the Coastal Ocean Monitoring Center, National Cheng Kung University, from 1998 to 2003. He has been an Assistant Professor at the Institute of Ocean Technology and Marine Affairs, National Cheng Kung University, since 2007. His research interests include ocean engineering, engineering statistics, ocean information management and statistical analysis, and system dynamics.

Li-Chung Wu received the Ph.D. degree in engineering from the National Cheng Kung University, Tainan, Taiwan, in 2008.

He has been an Assistant Research Fellow at the Coastal Ocean Monitoring Center, National Cheng Kung University, since 2008. His research interests include remote sensing, ocean engineering, image processing, and wavelet transform.